An Aerial Parallel Manipulator with Shared Compliance

Brett Stephens[1,2], Lachlan Orr[1,2], Basaran Bahadir Kocer[1], Hai-Nguyen Nguyen[3] and Mirko Kovac[1,2]

***Abstract*— Accessing and interacting with difficult to reach surfaces at various orientations is of interest within a variety of industrial contexts. Thus far, the predominant robotic solution to such a problem has been to leverage the maneuverability of a fully actuated, omnidirectional aerial manipulator. Such an approach, however, requires a specialised system with a high relative degree of complexity, thus reducing platform endurance and real-world applicability. The work here presents a new aerial system composed of a parallel manipulator and conventional, underactuated multirotor flying base to demonstrate interaction with vertical and non-vertical surfaces. Our solution enables compliance to external disturbance on both subsystems, the manipulator and flying base, independently with a goal of improved overall system performance when interacting with surfaces. To achieve this behaviour, an admittance control strategy is implemented on various layers of the flying base's dynamics together with torque limits imposed on the manipulator actuators. Experimental evaluations show that the proposed system is compliant to external perturbations while allowing for differing interaction behaviours as compliance parameters of each subsystem are altered. Such capabilities enable an adjustable form of dexterity in completing sensor installation, inspection and aerial physical interaction tasks. A video of our system interacting with various surfaces can be found here: https://youtu.be/38neGb8-lXg.**

I. Introduction

Aerial manipulators capable of physical interaction enable increased dexterity in manipulation and a larger workspace for tasks at height. As a result, these systems have the potential to yield significant benefits to infrastructure manufacturing, environmental sensing, transportation, and construction maintenance.

Recent work has provided an overview of the state-of-the-art in the field of aerial manipulation [1], [2]. From a hardware perspective, these flying platforms take form in a variety of configurations defined by their two primary subsystems: the flying base and the manipulator. Initial work in the field predominantly considered an underactuated flying base with a serial manipulator [3]–[5]. For these systems, work focused on the derivation of a suitable control allocation matrix to generate the desired wrench at the end-effector. Such work soon led to the development of fully actuated systems to physically interact with the environment in 6-DoF with multi-directional thrust capabilities [6]–[9]. However, these systems are mechanically more complex due to the additional hardware required for increased maneuverability. Such systems also lack endurance due to their increased mass and have lower thrust efficiency when the propellers are tilted in opposing directions [10].

Fig. 1: Stable orthogonal physical interaction on an inclined and/or angled target surface for: (1) an inclined target requiring the system to pitch; (2) an angled target requiring the system to reorient in yaw; (3) an inclined and angled target requiring the system to both pitch and reorient in yaw. When the target is angled, the flying base yaw reorientation strategy is utilized.

An alternative approach explored in recent studies is the use of parallel manipulators on aerial vehicles [11]–[14] which have the advantage of higher end-effector positional accuracy when compared to serial manipulators, as actuator angle uncertainties are averaged rather than summed, and generate smaller changes in the aerials manipulator's centre of mass (CoM) as the motors are mounted at the base and the linkages can be relatively lightweight. However, control of the end-effector position is often limited to stiff (i.e. non complaint) position setpoint control which limits interaction capabilities, especially with angled surfaces with an underactuated flying base. Furthermore, direct end-effector control is difficult with the underactuated quadrotor as a flying base, demanding a low level attitude controller as described in [15]. We therefore choose to control the CoM of our underactuated flying base and implement compliant parallel servos on the manipulator to facilitate stable behaviour during interaction.

In addition to various hardware configurations, novel control strategies have been explored in recent work. Initial solutions utilized a decoupled control approach by treating the manipulator and the base as entirely separate agents, with the flying base taking into account disturbances due to movement of the manipulator [16]. In more dynamic

[1]Aerial Robotics Laboratory, Imperial College London, London SW7 2AZ, UK. [2] Materials and Technology Center of Robotics at Empa, Swiss Federal Laboratories for Materials Science and Technology, Ueberlandstrasse 129, 8600 Dübendorf, Switzerland. [3] Laboratoire d'Analyse et d'Architecture des Systemes (LAAS), the Centre National de la Recherche Scientifique (CNRS), 7 Avenue du Colonel Roche, Toulouse, France.

motion, however, the distinct separation between these two subsystems may not satisfy requirements for a desired behaviour. A coupled approach considers the flying base and the manipulator as a single agent leveraging the full dynamic model of the system [17], [18]. The real-time solution of the fully coupled approaches requires the deployment of a model-based approach with full system dynamics. Such a requirement is computationally demanding, especially when the number of linkages in the manipulator are increased. Admittance control, which considers the aerial manipulator as a mechanical impedance, has been proposed for both the decoupled and coupled control approaches [19], [20] with applications including the peg-in-hole task [7], interaction with humans [21], collaborative drone transportation [22] and grasping with a multi-link drone [23].

In the work presented here, we aim to leverage the endurance and mechanical simplicity of the underactuated flying base with the precision and design benefits of a parallel manipulator to interact with the environment. The main distinction between our presented solution and the current state-of-the-art is our ability to expand the inherently limited workspace of the underactuated flying base with additional complaint linear and angular workspace degrees of freedom afforded by the manipulator. This hardware configuration is paired with a unique control strategy: utilizing multi-layer admittance control on various dimensions of the flying base's dynamics. We also develop and implement a reorientation approach at the attitude level of the system, enabling interaction with angled surfaces. While we treat our flying base and manipulator as decoupled entities from a control perspective, we implement the idea of shared compliance between the two subsystems: altering individual compliance parameters for each subsystem in order to "shape" the overall system compliance. The proposed system and methodology are validated for the sensor installation and inspection problem where a sustained force interaction is required. In summary, our work claims the following contributions:

- A new aerial manipulator hardware design, composed of an underactuated flying multirotor base and parallel manipulator robotic arm
- A decoupled and adjustable control approach to achieve desired interaction behaviour
- Experimental evaluations of our aerial manipulator, providing results for individual subsystem and total system performance under various conditions

A sample of our system's capabilities are illustrated in fig. 1, providing the foundations of an automated infrastructure inspection ecosystem.

II. System Description

The system configuration with the manipulator mounted forward of the propellers and above centre of mass is shown in fig. 3. The battery is attached at the rear of the system and its position can be adjusted to counterbalance the manipulator and any sensing payload on the end-effector.

The custom components for the manipulator were printed on a Markforged Mark Two carbon fibre composite printer. The actuators are Dynamixel XH-430 servo motors. The configuration of the manipulator and its degrees of actuation are illustrated in fig. 2. This configuration is based on the 2PRU+1PRS (2 prismatic revolute universal joint + 1 prismatic revolute spherical joint) manipulator described by Herrero Et al. [24]. This configuration has the advantage of limiting undesired parasitic motion to a single degree of freedom, along with the typical desirable properties of parallel manipulators such as high structural stiffness, low inertia and high accuracy due to the averaging of uncertainties of the positioning of each link. Smooth motion at universal joints $\mathbf{A}_1$, $\mathbf{A}_2$, $\mathbf{B}_1$ and revolute joints $\mathbf{B}_2$ and $\mathbf{B}_3$ is facilitated by rotary bearings set into the plastic. A spherical bearing is required at $\mathbf{A}_2$ to allow for the small amount of parasitic motion described by eq. (3).

The aerial base is controlled by a Pixhawk 4 flight controller with an Intel NUC (NUC7i7BNH) companion computer. A Vicon motion capture system is used to receive 6-DoF pose feedback at $100\,\mathrm{Hz}$. The mass of the aerial base, including the battery, is $3.01\,\mathrm{kg}$ and the mass of the manipulator is $518\,\mathrm{g}$ giving a total take-off mass of $3.53\,\mathrm{kg}$.

III. Modelling

The system is composed of two rigidly attached subsystems: a free floating quadrotor base and a rigidly attached manipulator. The coordinate frames used to describe the system can be seen in fig. 3, with $\mathcal{W}$ as an arbitrarily placed world frame, $\mathcal{B}$ as the body frame, rigidly attached to the flying base at the CoM, $\mathcal{M}$ as the manipulator base frame and lastly $\mathcal{E}$ as the frame fixed to the manipulator end-effector. The configuration of the base is described by

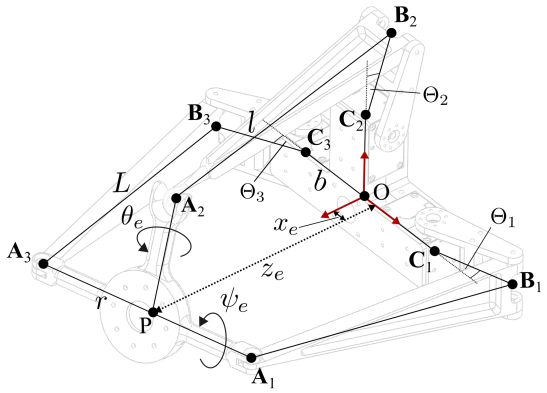

Fig. 2: Diagram of the parallel manipulator showing joint locations and degrees of freedom.

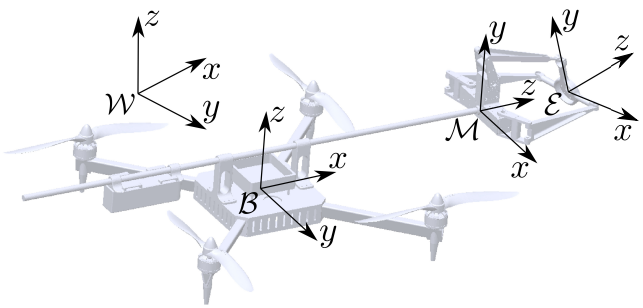

Fig. 3: Frame conventions for the flying base and the parallel manipulator.

the position vector ${}^{\mathcal{W}}\mathbf{p}_{\mathcal{B}} = [x\ y\ z]^T \in \mathbb{R}^3$ and rotation matrix ${}^{\mathcal{W}}\mathbf{R}_{\mathcal{B}} \in SO(3)$ parameterized by attitude in roll, ϕ, pitch, θ and yaw, ψ. The transformation of $\mathcal{M}$ in $\mathcal{B}$ can be described with a constant translation, ${}^{\mathcal{B}}\mathbf{p}_{\mathcal{M}} \in \mathbb{R}^3$, and orientation ${}^{\mathcal{B}}\mathbf{R}_{\mathcal{M}} \in SO(3)$.

The end-effector position ${}^{\mathcal{W}}\mathbf{p}_{\mathcal{E}} \in \mathbb{R}^3$ is calculated as:

$$ {}^{\mathcal{W}}\mathbf{p}_{\mathcal{E}} = {}^{\mathcal{W}}\mathbf{p}_{\mathcal{B}} + {}^{\mathcal{W}}\mathbf{R}_{\mathcal{B}}{}^{\mathcal{B}}\mathbf{p}_{\mathcal{M}} + {}^{\mathcal{W}}\mathbf{R}_{\mathcal{B}}{}^{\mathcal{B}}\mathbf{R}_{\mathcal{M}}{}^{\mathcal{M}}\mathbf{p}_{\mathcal{E}} \quad (1) $$

The rotation matrix of the end-effector, ${}^{\mathcal{W}}\mathbf{R}_{\mathcal{E}} \in SO(3)$, can be computed as:

$$ {}^{\mathcal{W}}\mathbf{R}_{\mathcal{E}} = {}^{\mathcal{W}}\mathbf{R}_{\mathcal{B}}{}^{\mathcal{B}}\mathbf{R}_{\mathcal{M}}{}^{\mathcal{M}}\mathbf{R}_{\mathcal{E}} \quad (2) $$

A. Kinematic Model

1) Flying Base: In this work, we model our flying base as a rigid body subject to gravity, possible external forces and torques as well as input control forces and torques. Control inputs are specific to the platform under examination: in this case, we leverage the well-known quadrotor, actuated via four fixed brushless DC motors generating a thrust vector $\mathbf{\Lambda} \in \mathbb{R}^3$ confined to the z-axis of the $\mathcal{B}$ frame. The configuration of the aerial base is described by the position and orientation of $\mathcal{B}$ with respect to $\mathcal{W}$, signified by position ${}^{\mathcal{W}}\mathbf{p}_{\mathcal{B}} \in \mathbb{R}^3$, and orientation ${}^{\mathcal{W}}\mathbf{R}_{\mathcal{B}} \in SO(3)$. Linear and angular velocities for the base are found using the same frame convention and are described with the following notation, respectively: ${}^{\mathcal{W}}\mathbf{v}_{\mathcal{B}} \in \mathbb{R}^3$ and ${}^{\mathcal{W}}\boldsymbol{\omega}_{\mathcal{B}} \in \mathbb{R}^3$.

2) Parallel Manipulator: Herrero Et al. [24] provides the inverse kinematic equations for a similar manipulator using linear actuators. The following derivation is based on this work, but has been adapted for rotary actuators. The manipulator has three desired degrees of freedom: translation in z_e and rotation in ψ_e and θ_e. There is an additional parasitic motion in x_e expressed as

$$ x_e = r \cdot s\theta_e s\psi_e. \quad (3) $$

Such movement is small in this configuration, however, and has a negligible affect on the applications presented here. The servo motor angles Θ_1, Θ_2 and Θ_3 must be expressed as a function of the desired end-effector states z_e, θ_e and ψ_e. The geometry is described by the end-effector radius, r, the base radius, b, proximal linkage length, l and distal linkage length, L.

The coordinates of the wrist joints $\mathbf{A}_i$ can be expressed in term of the desired end effector state and $\mathbf{B}_i$ in terms of the servo angles. The distance between them must be the length of the distal linkages, L, and so

$$ L^2 = \|\mathbf{A}_i\mathbf{B}_i\|^2 = \mathbf{A}_{ix}\mathbf{B}_{ix}^2 + \mathbf{A}_{iy}\mathbf{B}_{iy}^2 + \mathbf{A}_{iz}\mathbf{B}_{iz}^2. \quad (4) $$

To determine $\mathbf{A}_i\mathbf{B}_i$, the following loop-closure equation can be written:

$$ \mathbf{A}_i\mathbf{B}_i = \mathbf{OA}_i - \mathbf{OC}_i - \mathbf{C}_i\mathbf{B}_i. $$

Substituting expressions for $\mathbf{A}_i\mathbf{B}_i$, $\mathbf{OA}_i$, $\mathbf{OC}_i$ and $\mathbf{C}_i\mathbf{B}_i$ into Equation 4 produces

$$ a_i \sin\Theta_i + b_i \cos\Theta_i = c_i $$

where the values of the coefficients a_i, b_i, c_i are

$$ \begin{aligned} a_1 &= -z_e + rs\theta_e, \quad b_1 = -r\left(c\theta_e - s\phi_e s\theta_e\right) + b, \\ a_2 &= -z_e + rc\theta_e s\theta_e, \quad b_2 = -rc\phi_e + b, \\ a_3 &= -z_e - rs\theta_e, \quad b_3 = -r\left(c\theta_e + s\phi_e s\theta_e\right) + b, \\ c_i &= \frac{\left(L^2 - a_i^2 - b_i^2 - l^2\right)}{2l}. \end{aligned} $$

This can then be solved for the values of $\Theta_1, \Theta_2, \Theta_3$:

$$ \Theta_i = 2n\pi + \cos^{-1}\left(\frac{c_i}{\sqrt{a_i^2 + b_i^2}}\right) + \tan^{-1}\left(\frac{a_i}{b_i}\right). $$

Where $n \in \mathbb{Z}$. Setting $n = 0$ yields solutions in the desired actuation range of the servos between $-\frac{\pi}{2}$ and $\frac{\pi}{2}$. When computing this, an exception needs to be added for the case that $b_i = 0$ as $\lim_{b_i \to 0} \frac{a_i}{b_i} = \infty$. In this case $\lim_{b_i \to 0} \tan^{-1}\left(\frac{a_i}{b_i}\right) = \frac{\pi}{2}$ and so

$$ \Theta_i = \cos^{-1}\left(\frac{c_i}{a_i}\right) + \frac{\pi}{2}. $$

B. End Effector Workspace Analysis

The workspace of the manipulator can be calculated iteratively by testing whether valid solutions exist for varying end effector states. In fig. 4 the achievable values of θ_e, ψ_e and z_e are shown. The rotation of the end effector in ϕ_e is limited by collisions between the linkages and in θ_e by the rotational limits of the spherical joint at $\mathbf{A}_2$. To avoid these cases, the end effector rotations were limited to $\pm\frac{\pi}{4}$ radians and $0.13 \leq z_e \leq 0.22$. Some unattainable configurations still exist within these limits, however, they were not reached in the experiments performed here.

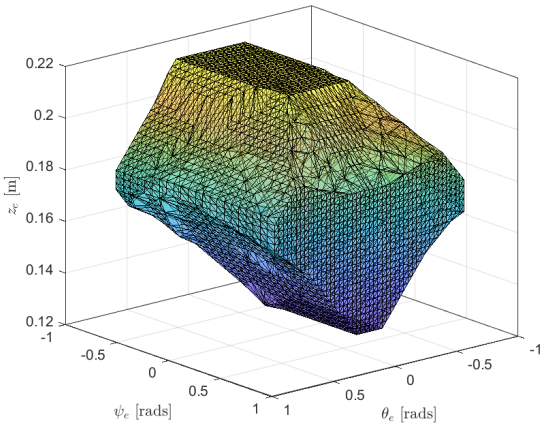

Fig. 4: The workspace of the manipulator, calculated numerically by determining the set of valid solutions to the inverse kinematics.

C. Dynamics

For the aerial manipulator shown in fig. 3, the linear and angular dynamics of the system can be written as follows:

$$ m\,{}^{\mathcal{W}}\dot{\mathbf{v}}_{\mathcal{B}} = -mg\mathbf{e}_3 + \lambda\,{}^{\mathcal{W}}\mathbf{R}_{\mathcal{B}}\ \mathbf{e}_3 + \mathbf{f}_e \quad (5) $$

$$ \begin{aligned} \mathbf{I}\ {}^{\mathcal{W}}\dot{\boldsymbol{\omega}}_{\mathcal{B}} &= S(\mathbf{I}\ {}^{\mathcal{W}}\boldsymbol{\omega}_{\mathcal{B}})\,{}^{\mathcal{W}}\boldsymbol{\omega}_{\mathcal{B}} + \boldsymbol{\tau} + \boldsymbol{\tau}_e \\ {}^{\mathcal{W}}\dot{\mathbf{R}}_{\mathcal{B}} &= {}^{\mathcal{W}}\mathbf{R}_{\mathcal{B}}\ S({}^{\mathcal{W}}\boldsymbol{\omega}_{\mathcal{B}}) \end{aligned} \quad (6) $$

Where $S(\cdot)$ is the skew-symmetric matrix operator such that $S(\mathbf{k})\boldsymbol{\nu} = \mathbf{k} \times \boldsymbol{\nu}$ for any generalized vectors $\mathbf{k}, \boldsymbol{\nu} \in \mathbb{R}^3$. $\mathbf{I} \in \mathbb{R}^{3\times3}$ is the quadrotor's inertia tensor, $\boldsymbol{\tau} \in \mathbb{R}^3$ is the control torque, $\mathbf{e}_3 = [0\ 0\ 1]^T$ is the z axis basis vector, λ is the thrust scalar of the base and g is the acceleration due to gravity.

Creating the state variable to describe the base's stacked linear and angular velocities as $\dot{\mathbf{q}} = [{}^{\mathcal{W}}\mathbf{v}_{\mathcal{B}}\ {}^{\mathcal{W}}\boldsymbol{\omega}_{\mathcal{B}}]^T$, the equations of motion from eq. (5) and eq. (6) can be rewritten in the well known Lagrangian form to describe the base as a rigid body in 3D space:

$$\mathbf{M}\ddot{\mathbf{q}} + \mathbf{C}(\dot{\mathbf{q}})\dot{\mathbf{q}} + \boldsymbol{\tau}_g = \mathbf{J}(\mathbf{q})\mathbf{F} + \mathbf{F}_e \tag{7}$$

where

$$\mathbf{M} = \begin{bmatrix} m\,\mathbb{I}_3 & \mathbf{0}_{3\times3} \\ \mathbf{0}_{3\times3} & \mathbf{I} \end{bmatrix}, \quad \mathbf{C}(\dot{\mathbf{q}}) = \begin{bmatrix} \mathbf{0}_{3\times3} & \mathbf{0}_{3\times3} \\ \mathbf{0}_{3\times3} & -S(\mathbf{I}\,{}^{\mathcal{W}}\boldsymbol{\omega}_{\mathcal{B}}) \end{bmatrix}$$

$$\boldsymbol{\tau}_g = \begin{bmatrix} mg\mathbf{e}_3 \\ \mathbf{0}_{3\times1} \end{bmatrix}, \quad \mathbf{J}(\mathbf{q}) = \begin{bmatrix} {}^{\mathcal{W}}\mathbf{R}_{\mathcal{B}} & \mathbf{0}_{3\times3} \\ \mathbf{0}_{3\times3} & \mathbb{I}_3 \end{bmatrix}$$

with $\mathbf{M} \in \mathbb{R}^{6\times6}$ describing the inertial effects of the system's mass, $\mathbf{C}(\dot{\mathbf{q}}) \in \mathbb{R}^{6\times6}$ capturing Coriolis forces, $\boldsymbol{\tau}_g \in \mathbb{R}^6$ as the gravity vector. $\mathbb{I}_n \in \mathbb{R}^{nxn}$ is the identity matrix of size n. The i^{th} propeller of the base rotates at angular velocity $\bar{\omega}_i \in \mathbb{R}$, allowing $\boldsymbol{\Omega} = [\bar{\omega}_1\ \bar{\omega}_2\ \bar{\omega}_3\ \bar{\omega}_4]^T$ to produce the control wrench $\mathbf{F} = \mathbf{B}\mathbf{u} = [\lambda\mathbf{e}_3\ \boldsymbol{\tau}]^T \in \mathbb{R}^6$, where $\mathbf{B} \in \mathbb{R}^{6\times4}$ is the control allocation matrix mapping control inputs $\mathbf{u} \in \mathbb{R}^4$ into generalized forces and torques. $\mathbf{F}_e = [\mathbf{f}_e\ \boldsymbol{\tau}_e]^T \in \mathbb{R}^6$ is the stacked external force and torque vectors exerted upon the system during interaction. As interaction with a target occurs over a small area, we assume single-point contact with target surfaces that generate a disturbance torque $\boldsymbol{\tau}_e \in \mathbb{R}^3$ described with force $\mathbf{f}_e \in \mathbb{R}^3$ and distance ${}^{\mathcal{B}}\mathbf{d}_{\mathcal{B}} \in \mathbb{R}^3$.

$$\boldsymbol{\tau}_e = {}^{\mathcal{W}}\mathbf{R}_{\mathcal{B}}\,{}^{\mathcal{B}}\mathbf{d}_{\mathcal{B}} \times \mathbf{f}_e \tag{8}$$

The aerial manipulator system highlighted here is designed such that the total system CoM is maintained within the body of the quadrotor base. Additionally, we assume relatively slow manipulator actuator movements resulting in low manipulator inertia, enabling us to treat the dynamics of the manipulator as a small perturbation to the flying base. We consider manipulator dynamics as quasi-static similar to [13], the derivation for which can be found in [24].

IV. Control

A. Flying base

In order to facilitate point-to-point translational motion of the base CoM, the well-known cascaded feedback control approach is taken to address the quadrotor's dynamics in two loops: the relatively low-speed outer translational loop and the high-speed inner attitude loop. We leverage the *differential flatness* [25] of the quadrotor's dynamics to control to a sufficiently smooth trajectory defined by the flying base's *flat* outputs characterized by the translational dimensions $[x, y, z]^T$ and yaw, ψ, as described in [26].

We proceed with developing a control law at the translational level of the quadrotor's dynamics to produce a desired thrust vector, $\boldsymbol{\Lambda} = \lambda\,{}^{\mathcal{W}}\mathbf{R}_{\mathcal{B}}\mathbf{e}_3 \in \mathbb{R}^3$ as a function of trajectory tracking errors, $\mathbf{e}, \dot{\mathbf{e}} \in \mathbb{R}^3$, from the base's dynamics described by linearizing eq. (7) about the hover configuration:

$$\boldsymbol{\Lambda} = \mathbf{M}_t\,{}^{\mathcal{W}}\dot{\mathbf{v}}^d_{\mathcal{B}} + \boldsymbol{\tau}_{g,t} - \mathbf{K}_d\dot{\mathbf{e}} - \mathbf{K}_p\mathbf{e} \tag{9}$$

where the $(\cdot)_t$ notation designates the translational portion of the respective matrix (i.e. $\mathbf{M}_t = m\mathbb{I}_3$, $\boldsymbol{\tau}_{g,t} = mg\mathbf{e}_3$), $(\cdot)^d$ is a desired parameter and $\mathbf{e} = {}^{\mathcal{W}}\mathbf{p}_{\mathcal{B}} - {}^{\mathcal{W}}\mathbf{p}^d_{\mathcal{B}}$. It can be shown that eq. (9) results in a closed-loop system described by linear error dynamics:

$$\mathbf{M}_t\ddot{\mathbf{e}} + \mathbf{K}_d\dot{\mathbf{e}} + \mathbf{K}_p\mathbf{e} = \mathbf{0}_{3\times1}$$

With the selection of appropriate positive definite gain matrices $\mathbf{K}_d, \mathbf{K}_p \in \mathbb{R}^{3\times3}$, the unperturbed (i.e. $\mathbf{f}_e = \mathbf{0}_{3\times1}$) closed-loop system is exponentially stable about the equilibrium point [27, Proposition 4.10]. While in contact with a target surface we rely upon the following for stable flight during interaction: 1) state feedback and appropriate control gain tuning to enforce desirable compliance to external perturbation and 2) enforcement of the constraint for small deviations from our translational equilibrium state (i.e. slow approach velocities). The stabilizing effect of such an approach can be seen in our experimental results. For theoretical guarantees on stability and passivity of underactuated aerial platforms under physical interactions, we refer the readers to the work in [28].

Following [29], the desired thrust vector from eq. (9) can be decomposed into its corresponding attitude commands. We begin by defining a thrust scalar command as $\lambda = \|\boldsymbol{\Lambda}\|$. The desired yaw, pitch, roll angles $[\psi^d\ \ \theta^d\ \ \phi^d]^T \in \mathbb{R}^3$ are computed with use of the parameterized rotation matrix $\mathbf{R} = \mathbf{R}_{e_3}(\psi)\mathbf{R}_{e_2}(\theta)\mathbf{R}_{e_1}(\phi)$ where $\mathbf{R}_{e_i}(\cdot)$ is the rotation matrix about the e_i-axis. The yaw angle ψ^d can then be chosen at will depending upon application.

The remaining attitude commands, roll and pitch, are then calculated as follows:

$$\mathbf{R}_{e_2}(\theta)\mathbf{R}_{e_1}(\phi)\mathbf{e}_3 = \begin{bmatrix} \sin\theta\cos\phi \\ -\sin\phi \\ \cos\theta\cos\phi \end{bmatrix} = \hat{\boldsymbol{\Lambda}}(\psi)$$

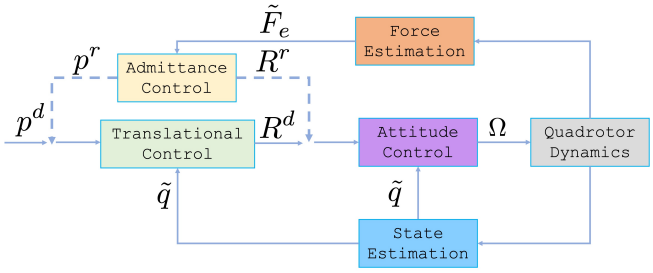

Fig. 5: The flying base's cascaded control architecture is shown here. Depending upon the desired behavior of the aerial manipulator, the modular architecture allows for the incorporation of admittance control at either the translational or attitude level of the quadrotor's dynamics.

where we defined the following relation as $\hat{\mathbf{\Lambda}}(\psi) = \frac{1}{\lambda}\mathbf{R}_{e_3}^T(\psi)\mathbf{\Lambda}$. We then can choose the roll and pitch commands as

$$\phi^d = -\sin^{-1}\hat{\Lambda}_2, \qquad \theta^d = \tan^{-1}\frac{\hat{\Lambda}_1}{\hat{\Lambda}_3},$$

with $\hat{\Lambda}_i$ as the ith element of $\hat{\mathbf{\Lambda}}$. The derived thrust scalar and attitude commands, $[\lambda \quad \psi^d \; \theta^d \; \phi^d]^T$ are then input to the inner-loop attitude controller. In practice, such an attitude controller takes the form of the PX4 open source flight controller.

1) Admittance Control: In our previous work [30], interactive capabilities were manifest via an admittance-based control scheme at the translational layer of the aerial base's dynamics, allowing for an intuitive response to an estimated external force perturbation $\tilde{\mathbf{f}}_e \in \mathbb{R}^3$. The resulting moment estimate about the vehicle's CoM, $\tilde{\boldsymbol{\tau}}_e \in \mathbb{R}^3$ can be calculated using the relation from eq. (8).

This admittance control strategy, constrained to the linear dynamics, proved relevant and effective for the simple interaction of a 1 DoF tool-tip with a vertical surface, resulting in a linear force acting in-line with the flying base's CoM. For the system designed here, however, the external force may act off-center relative to the platform's CoM and interaction with the environment may occur with non-vertical target surfaces. As such, it becomes evident that a more thorough control strategy should be considered. We introduce here an admittance control strategy capable of "shaping" the quadrotor's state:

$$\mathbf{M}_v\ddot{\mathbf{e}}[\star] + \mathbf{B}_v\dot{\mathbf{e}}[\star] + \mathbf{K}_v\mathbf{e}[\star] = \mathbf{F}_e[\star] \tag{10}$$

With $\mathbf{M}_v, \mathbf{B}_v, \mathbf{K}_v$ dictating the virtual dynamics of the reference trajectory and $\mathbf{e}[\star]$ signifying error of the relevant indices of the quadrotor's state. To give an example, if compliant behavior is desired on the translational level, the following relations hold for eq. (10):

$$\begin{aligned}\mathbf{M}_v, \mathbf{B}_v, \mathbf{K}_v &\in \mathbb{R}^{3\times 3}\\ \mathbf{e}[\star] &= ({}^{\mathcal{W}}\mathbf{p}_{\mathcal{B}}^d - {}^{\mathcal{W}}\mathbf{p}_{\mathcal{B}}^r)\\ \mathbf{F}_e[\star] &= \mathbf{f}_e\end{aligned}$$

Where $(\cdot)^r$ is a reference parameter generated as a function of sensed external force $\mathbf{f}_e$. The underactuated nature of the base makes the implementation of the control strategy in eq. (10) non-trivial, as modifications to the linear portion of control parameters $\mathbf{M}_v, \mathbf{B}_v$, and $\mathbf{K}_v$ will have an impact on the quadrotor's angular dynamics. The same phenomena holds vice versa. A visualization of this approach is presented in fig. 5, highlighting the ability to integrate compliance in a modular fashion within a cascaded control architecture: admittance can be implemented at the two layers of the system's dynamics (i.e. translational or attitude) together, independently or any combination thereof, though careful consideration of the base's dynamic coupling must be made when the combining these two layers. As such, the initial experiments discussed here focus on implementing our modular admittance control scheme on the translational and attitude layer independently.

Lastly, inspiration from [31] enables the unconventional implementation of an admittance controller, allowing the robot's state to be "shaped" by a desired state as opposed to an external wrench as was the case in eq. (10):

$$M_{q_i}\ddot{q_i}^r + B_{q_i}\dot{q_i}^r + K_{q_i}{q_i}^r = q_i \tag{11}$$

where q_i is the i^{th} component of $\mathbf{q}$ and M_{q_i}, B_{q_i} and K_{q_i} are the "shaping" control parameters. For the yaw dynamics, the control strategy defined by eq. (11) will instantiate as:

$$M_\psi\ddot{\psi}^r + B_\psi\dot{\psi}^r + K_\psi\psi^r = \psi \tag{12}$$

Here, reference yaw ψ^r is shaped by the current yaw ψ, allowing the quadrotor to reorient in the yaw dimension to its target surface as a function of virtual parameters M_ψ, B_ψ and K_ψ. Such behavior may be desirable if a sensor is required to be placed or held at an orthogonal angle to a target surface.

2) Force Estimation: Onboard force estimation is calculated via the accelerometer included in the Pixhawk 4 IMU. The base's translational dynamic equation from eq. (5) can be reformulated as $\mathbf{f}_e = m({}^{\mathcal{W}}\dot{\mathbf{v}}_{\mathcal{B}} + g\mathbf{e}_3) - \lambda^{\mathcal{W}}\mathbf{R}_{\mathcal{B}}\mathbf{e}_3$ where the $({}^{\mathcal{W}}\dot{\mathbf{v}}_{\mathcal{B}} + g\mathbf{e}_3)$ term represents the system's total acceleration. We then define ${}^{\mathcal{B}}\mathbf{a}_{\mathcal{B}} \in \mathbb{R}^3$ as the output of the Pixhawk 4 accelerometer and proceed with an estimate of the external force as:

$$\mathbf{f}_e = m{}^{\mathcal{W}}\mathbf{R}_{\mathcal{B}}{}^{\mathcal{B}}\mathbf{a}_{\mathcal{B}} - \lambda^{\mathcal{W}}\mathbf{R}_{\mathcal{B}}\mathbf{e}_3$$

where $\lambda^{\mathcal{W}}\mathbf{R}_{\mathcal{B}}\mathbf{e}_3 = \mathbf{\Lambda}$ is calculated using eq. (9) with velocity and position values generated from the state estimator. As the acceleromter data is characterized by high frequency oscillations, we implement a simple discrete low-pass filter that, for the i^{th} time step, takes the form:

$$\tilde{\mathbf{f}}_{e_i} = \alpha\mathbf{f}_{ei} + (1-\alpha)\tilde{\mathbf{f}}_{e_{i-1}}$$

with $\tilde{\mathbf{f}}_e \in \mathbb{R}^3$ as the filtered estimate and α, $0 \leq \alpha \leq 1$, the scalar smoothing factor, chosen empirically.

B. Manipulator

It is assumed that the end-effector position is accurately controlled via the manipulator's inverse kinematics (i.e. ${}^{\mathcal{M}}\mathbf{p}_{\mathcal{E}} \approx {}^{\mathcal{M}}\mathbf{p}_{\mathcal{E}}^d$), allowing for the precise knowledge of the end-effector position via eq. (1).

The inverse kinematics allows the conversion of the end effector's desired displacement (z_e), pitch angle (θ_e) or yaw angle (ψ_e) to the corresponding angles of the three servo motors. These angle commands are passed to each of the three Dynamixel servos where position and velocity trajectories are generated on-board to smoothly move to the commanded angle. A PID controller with additional velocity and acceleration feed-forward terms calculates the required PWM output to drive the motor. Compliance to external perturbation on the manipulator is enabled via current-limiting control, wherein the PWM output is limited to avoid exceeding a threshold current draw for the motor. Such a strategy limits the force/torque that can be exerted at the end effector.

V. Experimental Evaluation

Flight experiments have been performed to characterise the performance of the aerial manipulator and flying base as separate entities and as a total system.

A. String Pull

The experiments performed here take form of "string-pull" tests: while the aerial manipulator is in a hover state, an external perturbation is introduced via a string attached to the aerial manipulator's CoM in order to quantify how our cascaded admittance control approach behaves on each dynamic layer of the system. It is the intent of these experiments to characterise the compliance of our proposed control strategy to external perturbation. Admittance was implemented either on the translational layer or the attitude layer, but not both simultaneously. In fig. 6, a force in the y direction is exerted upon the system. The translational admittance scheme is clearly validated in the y dimension as the external force $f_{e,y}$ "shapes" the y position of the flying base as a function of the gain parameters. Keeping all other parameters static, the $\mathbf{K}_v$ gain was adapted from a value of 25 to 5 in order to highlight the behavior of a "stiff" and "soft" system, respectively. Under external force $f_{e,y}$, the system's remaining translational dynamics (i.e. in x and z) remain static as a function of time.

A similar string pull experiment was performed on the attitude dynamic layer, specifically in the yaw dimension. Yaw compliance to a torque about the z-axis, $\tau_{e,z}$, is shown in fig. 7. Similar behaviour to the translational string pull test can be seen on the attitude level.

Lastly, the ability of our modular admittance strategy to shape a reference yaw, ψ^r, to the current yaw, ψ, is depicted in fig. 8. Here, it can be clearly seen that the base is able to reorient according to the current yaw, a feature which affords the base an ability to reorient during interactions with variable geometry surfaces.

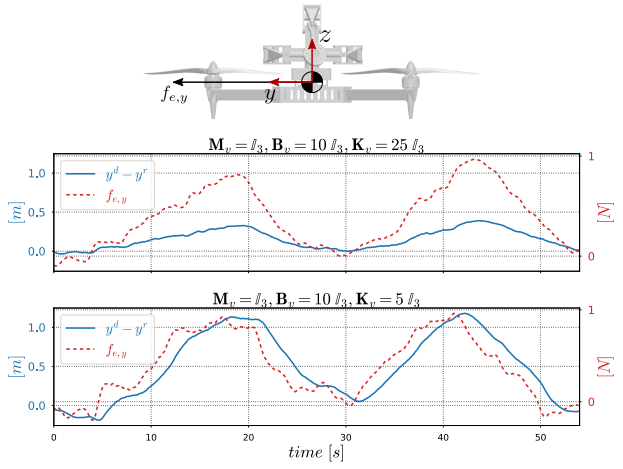

Fig. 6: The translational base admittance controller is "shaped" by an external force in the y-direction, $f_{e,y}$. Intuitive positional behavior is observed as the "stiff" system ($\mathbf{K}_v = 25\ \mathbb{I}_3$) is less compliant to $f_{e,y}$ relative to the "soft" system ($\mathbf{K}_v = 5\ \mathbb{I}_3$). Force values have been normalized.

B. Shared Compliance

Next, initial experiments are performed to determine total system interaction behaviour when in contact with a target. The intent of these experiments is to understand the overall system compliance during interaction by varying the compliance parameters for each subsystem.

A vertical target was placed at an orthogonal orientation relative to the x axis with a desired position $x^d(t)$ defined behind the target to facilitate interaction. In these experiments, the translational admittance compliance parameters for the flying base are $\mathbf{M}_v = \mathbb{I}_3$, $\mathbf{B}_v = 10\mathbb{I}_3$, $\mathbf{K}_v = 25\mathbb{I}_3$, chosen due to their favourable behavior during our previously conducted string pull tests. The "stiff" case for the base deactivates the base's admittance control scheme, removing the base's ability to adjust its translational state to a sensed force. For the manipulator, the compliant setting defines the actuator torque limit at $0.06\,\mathrm{Nm}$ and the "stiff" setting defines this torque limit at $0.28\,\mathrm{Nm}$. Unlike the base, the manipulator has no force feedback and therefore behaves much like a mechanical spring with an adjustable spring constant fixed to the flying base. A higher torque limit on the servo motors corresponds to a stiffer spring in this analogy.

We test two compliance parameter sets for the base: a

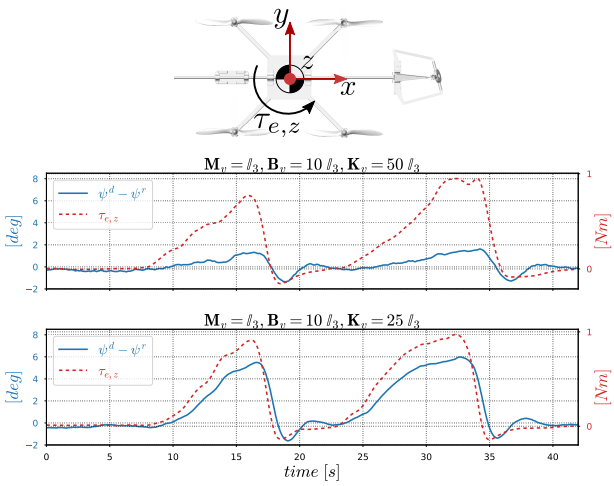

Fig. 7: The base's attitude admittance controller is "shaped" by an external torque about the z-axis, $\tau_{e,z}$ for two differing values of $\mathbf{K}_v$: 50 $\mathbb{I}_3$ and 25 $\mathbb{I}_3$. Reported torque values are normalized.

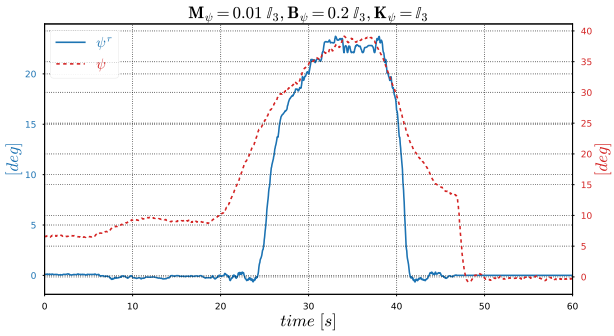

Fig. 8: The base's reference yaw, ψ^r, is "shaped" by the current yaw, ψ. Such a strategy allows for the flying base to reorient to target surfaces of various orientations.

"stiff" base represented by the variable b_s and a compliant base represented by the variable b_c, against the two different compliance parameter sets for the manipulator: a "stiff" manipulator represented by variable m_s and a compliant manipulator represented by m_c. As the target is positioned to perturb the system along the x axis of ${}^{\mathcal{W}}\mathbf{p}_{\mathcal{B}}$, we focus upon the position $x(t)$ for each test case in relation to $x^d(t)$. When the flying base is stiff, the system has no force feedback and therefore produces a larger thrust in an attempt to reach the desired target point $x^d(t)$. This manifests as $x(t) - x^d(t)$ being relatively small during contact. In the case of a compliant base, however, the base is "pushed" back by the sensed external force $f_{e,x}$ exerted upon the system by the target surface, resulting in a reference position that is "shaped" by the selected compliance parameters. Such an effect manifests as $x(t) - x^d(t)$ being relatively large during contact.

We then investigate the effects of the manipulator on the overall system compliance. When the compliant manipulator is activated, the system behaves as if there is a spring, fixed to the base and terminating at the end-effector, allowing the system to traverse relatively close to the desired position $x^d(t)$ and thus making $x(t) - x^d(t)$ smaller. The opposite is true for the "stiff" manipulator, which inhibits the base from reaching the desired state, resulting in a larger $x(t) - x^d(t)$ during contact. The combined effects of the behaviour described here can be seen in fig. 9, with the base's compliance dominating the overall system positional behavior due to its ability to react to sensed forces.

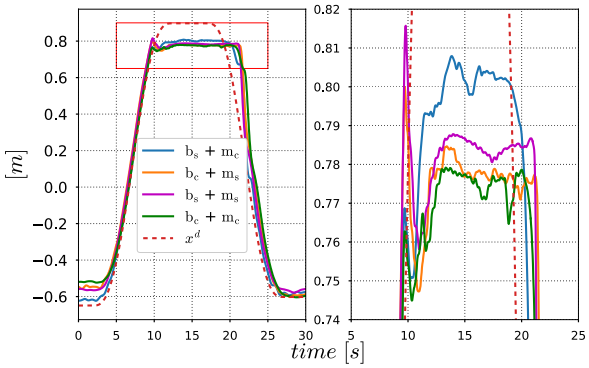

Fig. 9: Vertical wall interaction experiments with varying compliance parameter sets (i.e. "stiff" $(\cdot)_s$ and compliant $(\cdot)_c$) for the flying base and the parallel manipulator. A magnified portion of the left plot, outlined with the red box, is shown in the right plot. The high amplitude spike in $x(t)$ at $t \approx 10\,\mathrm{s}$ is due to the end-effector initiating contact with the target surface.

C. Angled Surface Interaction

Initial experiments are performed to quantify our ability to reorient the base to an angled target by implementing the yaw admittance scheme from eq. (12). Relative to the approach motion in the x direction, the target surface is angled about the z axis at $\approx 15°$. It is noted that the the desired position x^d is located behind the target surface, resulting in the discrepancy between x and x^d during contact.

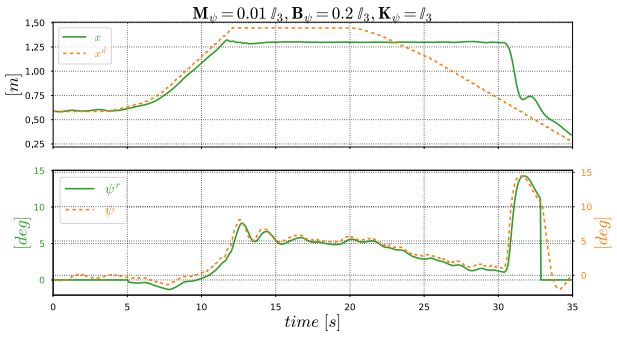

Fig. 10: The aerial manipulator approaches an angled surface in the x direction in the top plot. The bottom plot illustrates our ability to reorient the flying base in yaw ψ when in contact with an angled surface.

Looking at fig. 10, the yaw admittance scheme is activated at $t \approx 5\,\mathrm{s}$. The system approaches the target and makes contact at $t \approx 12\,\mathrm{s}$. At this time, the base begins to reorient in the direction of the angled surface with the reference yaw ψ^r following the state yaw ψ, reaching a "steady-state" yaw angle of $\approx 6°$. From $t \approx 23\,\mathrm{s}$ to $t \approx 30\,\mathrm{s}$ the system is commanded to detach from the target, though the magnetic end-effector has not yet released from the surface. The magnet releases at $t \approx 31\,\mathrm{s}$ resulting in a relatively large yaw perturbation. Such behavior can be mitigated by replacing the permanent magnet with an electromaget to faciltate smooth departure motion. The yaw admittance controller is then disengaged at $t \approx 33\,\mathrm{s}$ and the reference yaw ψ^r returns to 0.

Despite a target orientation of $\approx 15°$, it can be seen that the base only reorients to $\approx 6°$. This is due to the values chosen for M_ψ, B_ψ, K_ψ, which can be adjusted if further reorientation is desired.

D. Trajectory Tracking

Next, trajectory tracking and sensor placement accuracy tests are conducted and summarized in table I for a total of 16 trails on a vertical surface. Trajectory tracking is quantified for free-flight (i.e. non interactive) motion as the aerial manipulator approaches the target. It can be seen that highly accurate tracking is achieved with an average mean squared error of less than $3.5\,\mathrm{cm}$ over all dimensions. The average absolute error of the end-effector position, ${}^{\mathcal{W}}\mathbf{p}_{\mathcal{E}}$, relative to the desired end-effector position, ${}^{\mathcal{W}}\mathbf{p}^d_{\mathcal{E}}$, is also reported as the sensor placement error relative to a target at $y, z = (0, 0)$ [cm]. Comparing these two metrics, it becomes evident that despite highly accurate trajectory tracking, the sensor placement position error is relatively large. Such a discrepancy is likely due to the end-effector moving relative to the target upon initial contact, resulting in additional error, especially along the z axis. The permanent magnet fixed on

TABLE I: Trajectory tracking error results for 16 trials.

Trajectory Tracking MSE [cm]			**Sensor Placement Error [cm]**	
x	y	z	y	z
1.803	0.102	3.390	2.157	11.166

the end-effector also effects placement error, fixing the end-effector position once contact is made.

VI. Conclusions

We have presented a shared compliance mechanism for aerial physical interaction using an underactuated flying base with a new parallel manipulator configuration. We demonstrated our system's ability to track trajectories for accurate target interaction and maintain compliance at various levels of the system's dynamics. Our system's ability to manifest compliance at both the base and manipulator allowed for robust interaction with vertical and angled surfaces.

This work forms the foundation for aerial contact-based interactions that can be applied to inspection and sensor installation in industrial and natural environments. Future extensions of this work will investigate implementing admittance control strategies on various levels of the base's dynamics simultaneously as well as integrating object detection techniques required to develop trajectories and locate viable target surfaces. Furthermore, reactive collision prevention will be considered in the system (e.g. optical flow based) as an additional safety loop [32].

Acknowledgment

This work was supported by funding from EPSRC (award no. EP/N018494/1, EP/R026173/1, EP/R009953/1, EP/S031464/1, EP/W001136/1), NERC (award no. NE/R012229/1) and the EU H2020 AeroTwin project (grant ID 810321). Mirko Kovac is supported by the Royal Society Wolfson fellowship (RSWF/R1/18003). We would like to thank Raihaan Usman for his support in generating high-quality images of our aerial manipulator.

References

[1] F. Ruggiero, V. Lippiello, *et al.*, "Aerial manipulation: A literature review," *IEEE Robotics and Automation Letters*, vol. 3, no. 3, pp. 1957–1964, 2018.

[2] A. Ollero, M. Tognon, *et al.*, "Past, present, and future of aerial robotic manipulators," *IEEE Transactions on Robotics*, 2021.

[3] S. Kim, S. Choi, *et al.*, "Aerial manipulation using a quadrotor with a two dof robotic arm," in *IEEE/RSJ International Conference on Intelligent Robots and Systems*, 2013, pp. 4990–4995.

[4] A. Santamaria-Navarro, P. Grosch, *et al.*, "Uncalibrated visual servo for unmanned aerial manipulation," *IEEE/ASME Transactions on Mechatronics*, vol. 22, no. 4, pp. 1610–1621, 2017.

[5] A. Suarez, F. Real, *et al.*, "Compliant bimanual aerial manipulation: Standard and long reach configurations," *IEEE Access*, vol. 8, pp. 88 844–88 865, 2020.

[6] M. Kamel, S. Verling, *et al.*, "The voliro omniorientational hexacopter: An agile and maneuverable tiltable-rotor aerial vehicle," *IEEE Robotics & Automation Magazine*, vol. 25, no. 4, pp. 34–44, 2018.

[7] M. Ryll, G. Muscio, *et al.*, "6d interaction control with aerial robots: The flying end-effector paradigm," *The International Journal of Robotics Research*, vol. 38, no. 9, pp. 1045–1062, 2019.

[8] K. Bodie, M. Brunner, *et al.*, "An omnidirectional aerial manipulation platform for contact-based inspection," in *Robotics: Science and Systems*, 2019.

[10] P. Zheng, X. Tan, *et al.*, "Tiltdrone: A fully-actuated tilting quadrotor platform," *IEEE Robotics and Automation Letters*, vol. 5, no. 4, pp. 6845–6852, 2020.

[9] M. Á. Trujillo, J. R. Martínez-de Dios, *et al.*, "Novel aerial manipulator for accurate and robust industrial ndt contact inspection: A new tool for the oil and gas inspection industry," *Sensors*, vol. 19, no. 6, p. 1305, 2019.

[11] P. Chermprayong, K. Zhang, *et al.*, "An integrated delta manipulator for aerial repair: A new aerial robotic system," *IEEE Robotics & Automation Magazine*, vol. 26, no. 1, pp. 54–66, 2019.

[12] D. Tzoumanikas, F. Graule, *et al.*, "Aerial manipulation using hybrid force and position nmpc applied to aerial writing," in *Robotics: Science and Systems*, 2020.

[13] K. Bodie, M. Tognon, *et al.*, "Dynamic end effector tracking with an omnidirectional parallel aerial manipulator," *IEEE Robotics and Automation Letters*, vol. 6, no. 4, pp. 8165–8172, 2021.

[14] B. B. Kocer, L. Orr, *et al.*, "An intelligent aerial manipulator for wind turbine inspection and repair," in *UKACC International Conference on Control*, 2022, pp. 226–227.

[15] H. Nguyen, C. Ha, *et al.*, "Mechanics, control and internal dynamics of quadrotor tool operation," *Automatica*, vol. 61, pp. 289–301, 2015.

[16] F. Ruggiero, M. A. Trujillo, *et al.*, "A multilayer control for multirotor uavs equipped with a servo robot arm," in *IEEE International Conference on Robotics and Automation*, 2015, pp. 4014–4020.

[17] A. Y. Mersha, S. Stramigioli, *et al.*, "Exploiting the dynamics of a robotic manipulator for control of uavs," in *IEEE international conference on robotics and automation*, 2014, pp. 1741–1746.

[18] C. Korpela, M. Orsag, *et al.*, "Towards valve turning using a dual-arm aerial manipulator," in *IEEE/RSJ International Conference on Intelligent Robots and Systems*, 2014, pp. 3411–3416.

[19] F. Forte, R. Naldi, *et al.*, "Impedance control of an aerial manipulator," in *American Control Conference*, 2012, pp. 3839–3844.

[20] F. Augugliaro and R. D'Andrea, "Admittance control for physical human-quadrocopter interaction," in *European Control Conference*, 2013, pp. 1805–1810.

[21] S. Rajappa, H. Bülthoff, *et al.*, "Design and implementation of a novel architecture for physical human-uav interaction," *The International Journal of Robotics Research*, vol. 36, no. 5-7, pp. 800–819, 2017.

[22] A. Tagliabue, M. Kamel, *et al.*, "Robust collaborative object transportation using multiple mavs," *The International Journal of Robotics Research*, vol. 38, no. 9, pp. 1020–1044, 2019.

[23] F. Shi, M. Zhao, *et al.*, "Aerial regrasping: Pivoting with transformable multilink aerial robot," in *IEEE International Conference on Robotics and Automation*, 2020, pp. 200–207.

[24] S. Herrero, C. Pinto, *et al.*, "Analysis of the 2PRU-1PRS 3DOF parallel manipulator: kinematics, singularities and dynamics," *Robotics and Computer-Integrated Manufacturing*, vol. 51, pp. 63–72, jun 2018.

[25] M. J. Van Nieuwstadt and R. M. Murray, "Real-time trajectory generation for differentially flat systems," *International Journal of Robust and Nonlinear Control*, vol. 8, no. 11, pp. 995–1020, 1998.

[26] D. Mellinger, "Trajectory Generation and Control for Quadrotors," *2011 IEEE International Conference on Robotics and Automation*, pp. 2520–2525, 2011.

[27] R. M. Murray, Z. Li, *et al.*, *A mathematical introduction to robotic manipulation*. CRC press, 2017.

[28] T. Tomić, C. Ott, *et al.*, "External wrench estimation, collision detection, and reflex reaction for flying robots," *IEEE Transactions on Robotics*, vol. 33, no. 6, pp. 1467–1482, 2017.

[29] H. Nguyen, S. Park, *et al.*, "A novel robotic platform for aerial manipulation using quadrotors as rotating thrust generators," *IEEE Transactions on Robotics*, vol. 34, no. 2, pp. 353–369, 2018.

[30] B. Stephens, H. Nguyen, *et al.*, "An integrated framework for autonomous sensor placement with aerial robots," *Transactions on Mechatronics*.

[31] K. Patnaik, S. Mishra, *et al.*, "Design and Control of SQUEEZE: A Spring-augmented QUadrotor for intEractions with the Environment to squeeZE-and-fly," *IEEE International Conference on Intelligent Robots and Systems*, pp. 1364–1370, 2020.

[32] F. Xiao, P. Zheng, *et al.*, "Optic flow-based reactive collision prevention for mavs using the fictitious obstacle hypothesis," *IEEE Robotics and Automation Letters*, vol. 6, no. 2, pp. 3144–3151, 2021.